Chemical Engineering Journal 512 (2025) 161930

Contents lists available at ScienceDirect

Chemical Engineering Journal

journal homepage: www.elsevier.com/locate/cej

Electrostatic-Induced Crystal-Rearrangement of Benzoquinones Cathode for Large-Scale All-Organic Aqueous Proton Batteries

Jianyong Zhang [a], Jingyuan Yu [a], Wenwei Zhang [a], Ahmed Eissa Abdelmaoula [e], Chunhua Han [a], Zhenzhen Dou [a,*], Feng Liang [b,*], Lin Xu [a,c,d,f,*]

[a] State Key Laboratory of Advanced Technology for Materials Synthesis and Processing, School of Materials Science and Engineering, Wuhan University of Technology, Wuhan 430070, China
[b] The Faculty of Metallurgical and Energy Engineering, Kunming University of Science and Technology, Kunming 650093, China
[c] Hubei Longzhong Laboratory, Wuhan University of Technology (Xiangyang Demonstration Zone), Xiangyang 441000, China
[d] Hainan Institute, Wuhan University of Technology, Sanya 572000, China
[e] Mining and Metallurgical Department, Faculty of Engineering, Al-Azhar University, Cairo 11884, Egypt
[f] Zhongyu Feima New Material Technology Innovation Center (Zhengzhou) Co., Ltd., Zhengzhou 450001, China

ARTICLE INFO

Keywords:
Proton battery
Proton energy storage
Hydrogen bonding coupling
Molecular regulation
Crystal rearrangement

ABSTRACT

Organic electrodes showcase promising perspectives in aqueous batteries for their environmental friendliness, renewability, and recyclability. However, the conundrum of achieving molecular scale regulation to improve the conductivity of organic materials via simplistic methods remains a challenge. Herein, we propose a facile electrostatic-induced crystal rearrangement (EICR) strategy to manipulate the molecular regulation of organic electrodes at the molecular level, thus enhancing their conductivity. This strategy follows the "hydrogen bonding coupling" mechanism, being confirmed by the molecular interaction between C=O and N-H in DFT, the ^{1}H spectrum shift in NMR, and the stretching of atomic distances between C and O, N and H in PDF and FTIR. More importantly, this work, for the first time, attains the highest capacity (264 mAh) proton pouch cell among current reports, which proffers the promising potential for large-scale applications of organic electrodes in aqueous proton batteries (PBs) and presents an unprecedented advancement for the practical application of PBs.

1. Introduction

Due to the merits of high safety and environmental friendliness, aqueous batteries (ABs) are regarded as one of the most promising candidates for large-scale energy storage. In numerous ABs, such as H^+ (with a radius of ~ 0.89 fm), Li^+ (76 pm), Na^+ (102 pm), K^+ (138 pm), Ca^{2+} (112 pm), Mg^{2+} (72 pm), Zn^{2+} (74 pm), Fe^{2+} (61 pm), Mn^{2+} (81 pm), Al^{3+} (54 pm), Cd^{2+} (95 pm), NH_4^+ (148 pm), H_3O^+ (~100 pm) ion batteries (femtometer = 10^{-15} m, picometer = 10^{-12} m)[1–3], proton (H^+) batteries (PBs) have the lowest ionic radius with high dynamic properties, abundant resources with extremely low costs, dendrite-free properties with high safety[4]. Hence, PBs deliver promising perspectives that have ushered in unprecedented development in the past few years[5–12]. In PBs, considerable efforts have been made to facilitate the intrinsic electronic conductivity of organic electrodes[13–33]. The poor conductivity of organic electrodes leads to low capacity and undesirable energy density[13,34–36], thereby drastically restraining the extensive implementation of organic electrodes in the energy storage domain of PBs.

Regulating the organic electrodes with enhanced conductivity is of utmost necessity and urgency in the large-scale energy storage of PBs. Currently, considerable efforts are being made to enhance the conductivity of organic-type benzoquinone (BQ) electrodes[14–16,37–42], which can be divided into two categories. One stratagem is adding conductive carbonaceous materials such as nanoporous carbon[17], zeolite-templated carbon[18], porous carbon[43], and porous rGO foam [39]. However, carbonaceous additives take up a high volume of electrodes, leading to low capacity and energy density. Another stratagem is grafting conductive polymers onto the electrodes, including PEDOT [13,23], EDOT[22], PN-AQ[15], pDTP-AQ[24], PEO/PPO-BQ[25], and EPE-NQ[26]. Whereas, the synthesis of conductive polymer grafted quinones needs a long-winded and intricate process. For example, the synthesis of EDOT-BQ requires more than ten types of additive materials and the synthesis process consists of over seven rigmarole procedures.

* Corresponding authors.
E-mail addresses: dzz0881@whut.edu.cn (Z. Dou), liangfeng@kust.edu.cn (F. Liang), linxu@whut.edu.cn (L. Xu).

https://doi.org/10.1016/j.cej.2025.161930
Received 11 December 2024; Received in revised form 17 March 2025; Accepted 23 March 2025
Available online 27 March 2025

Furthermore, the synthesis of EDOT-BQ needs toxic additives (DCM, BBr_3)[13], and these additives have to be removed for the further purification of the product. As a result, the synthesis of EDOT-BQ displays high costs and a prolix procedure, which makes it unsuitable for the large-scale application of PBs. Facile approaches have barely been developed for the conductivity improvement of organic electrodes with molecular regulation in PBs. Therefore, it is of paramount importance to explore a facile, and economical strategy involving molecular regulation to enhance the intrinsic electronic conductivity of organic electrodes, which holds profound significance for large-scale energy storage in PBs.

Herein, we present a facile EICR strategy mediated by hydrogen bonding coupling at the molecular level, aiming to augment the conductivity of organic electrodes, thereby proffering the referable instruction and theoretical foundation for molecular regulation of organic materials. The formation of EICR is caused by hydrogen bonding coupling between the C=O in BQ and the N-H bonds in polyaniline (PANI), which is evinced by the fact that the ^{1}H spectrum (~7.18 ppm) shifts to a low position in nuclear magnetic resonance (NMR). The analysis results of low bonding energy (−0.417 eV) between the C=O and the N-H bonds in density functional theory (DFT) and stretching of atomic distances between C and O of BQ in PDF (Pair distribution function, offering atom distance information in compounds) further attest the existence of hydrogen bonding coupling in PANI-BQ (P-BQ) electrodes. A vibration of the N-H bond around 1620 cm^{-1} is observed in FTIR, which further provides cogent evidence for hydrogen bonding coupling in P-BQ. Notably, this molecular-level manipulation successfully rearranges the original non-conductive crystal structure of the electrode to a conductive one via the hydrogen bonding coupling between the BQ and polyaniline (PANI), resulting in a significant reduction in electrochemical polarization from △0.19 V to △0.15 V and charge-transfer interfacial resistance from 28 Ω to 3.2 Ω. It has been demonstrated that the addition of PANI effectively prevents BQ from forming large-size crystallized particles and promotes the rearrangement of BQ molecules, thus enhancing the conductivity of the BQ. Most importantly, for the first time, we realized an all-organic proton pouch cell P-BQ//H_2SO_4//P-2ClAQ with a capacity of 264 mAh, which is the highest capacity among current reports in PBs. This work presents a simplistic strategy for augmenting the conductivity of organic electrodes and unveils the underlying scientific mechanism of the EICR strategy, which provides a significant theoretical foundation for molecular regulation and offers a practicable example for the large-scale application of energy storage in PBs.

2. Results and Discussion

2.1. Unraveling the synthesis and hydrogen bonding coupling configuration of P-BQ

As depicted in Fig. 1a, the synthesis of BQ is achieved facilely by incorporating PANI and BQ into an N-methylpyrrolidone (NMP) solution. Subsequently, upon drying, P-BQ is obtained. The inspiration for the synthesis of the P-BQ electrode comes from the traditional electrode preparation process. In traditional electrode synthesis, the PVDF (Polyvinylidene Fluoride) is dissolved in an NMP solution and is stretched to be a long chain to bind the electrode materials. We hypothesized that the PANI could be dissolved by NMP and could integrate with the BQ electrode in NMP. Consequently, we attempted to mix the PANI and BQ in an NMP solution and observed that both materials can be thoroughly dissolved in NMP and form a homogeneous slurry. The uniform slurry can be directly coated on the titanium current collector to fabricate a

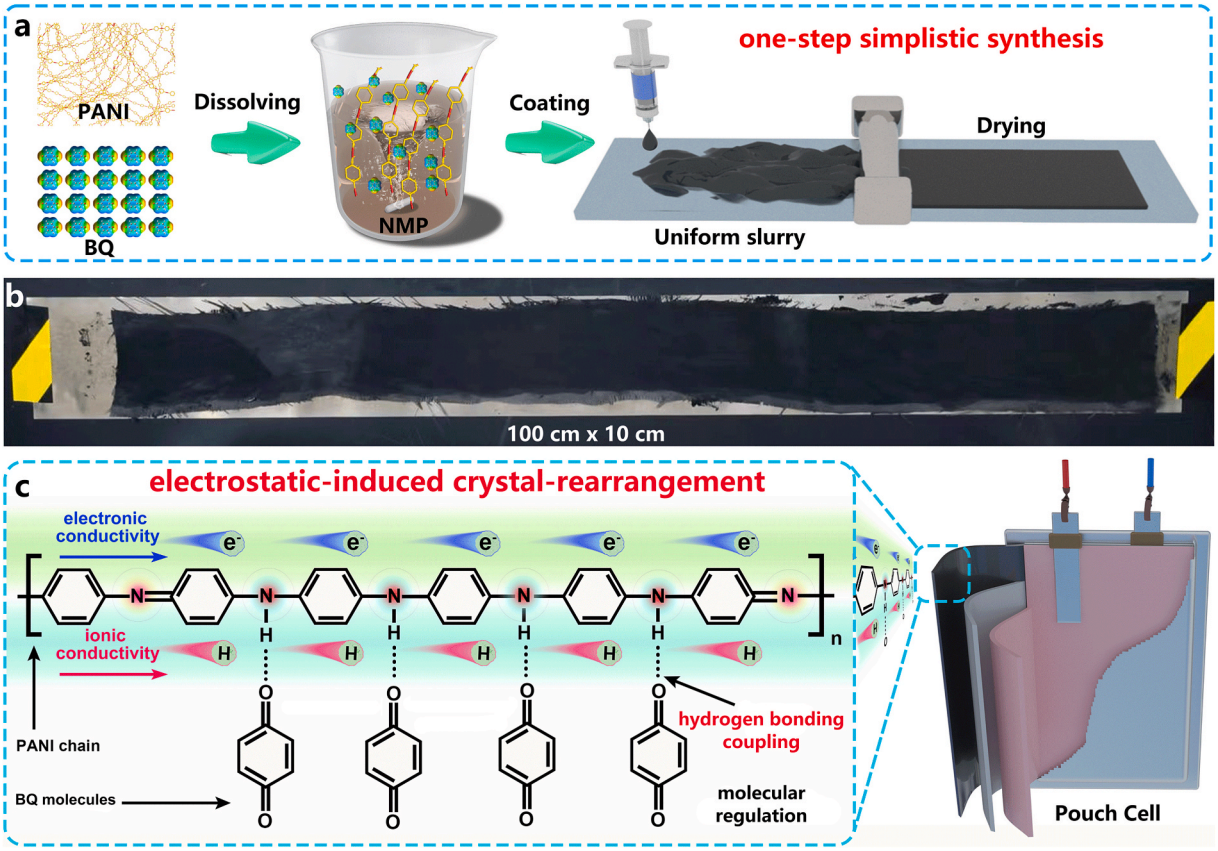

Fig. 1. Schematic depiction of P-BQ synthesis and the hydrogen bonding coupling configuration in P-BQ with a pouch cell. (a) Schematic illustration of the synthesis for P-BQ electrode. (b) Digital photo of large-area P-BQ electrode (100 cm × 10 cm). (c) Schematic illustration of hydrogen bonding coupling configuration in P-BQ with a pouch cell.

large-size electrode (Fig. 1b, 100 cm × 10 cm). Such a stratagem significantly shortens the synthesis procedure of organic electrodes in traditional reports and represents the promising potential for the large-scale application of organic-type electrode preparation.

Further, to corroborate the formation of hydrogen bonding coupling between BQ and PANI, the DFT calculation is applied to calculate the interaction between BQ and PANI. The DFT calculation results have certified that the BQ is grafted with PANI chains via the electrostatic attraction between C=O and N-H (Fig. S1), which is proved by the evidence that the bonding energy (the bond energies of the C=O group with N-H and C-H groups) is low (−0.417 eV < −0.214 eV) and the bond distance (ditto) is short (1.845 Å < 2.949 Å). This calculation result discloses that BQ molecules are attracted around the PANI chains via the hydrogen bonding coupling between C=O and N-H instead of C=O and C-H (Fig. S1). The energy level of BQ was changed to a low (−0.417 eV) and stable position shown in Fig. S1a instead of high position −0.214 eV (Fig. S1b). The total density of states (TDOS) of BQ has a band gap of 0.34 eV (Fig. S1c), showing relatively poor electrical conductivity. In contrast, the TDOS of P-BQ (Fig. S1d) has no bond gap, indicating metallic properties and thus excellent electrical conductivity. The PANI chains impart both electronic conductivity and ionic conductivity to the BQ molecule as showcased in Fig. 1c. Consequently, the P-BQ material exhibits a rearranged conductive configuration at the molecular level with hydrogen bonding coupling, efficaciously enhancing the conductivity of BQ electrodes.

To attest the existence of hydrogen bonding coupling between C=O and N-H, nuclear magnetic resonance (NMR) spectroscopy was employed to study the ^{1}H NMR characteristics within P-BQ. In addition, PANI is added to BQ with five different mass ratios (0 %, 25 %, 50 %, 75 %, 100 %) to investigate the influence of PANI addition on BQ, and the five samples are abbreviated as P-BQ-0 %, P-BQ-25 %, P-BQ-50 %, P-BQ-75 %, and P-BQ-100 %. It is noteworthy that the P-BQ-0 % sample constitutes pure BQ, while the P-BQ-100 % sample consists of pure PANI. The design of this experimental setup is aimed at comparing the disparity in properties between the pristine materials and the P-BQ materials. As depicted in Fig. S2, the ^{1}H spectrum (~7.18 ppm), which is associated with the hydrogen in N-H groups, undergoes a gradual shift towards lower chemical shift values with the samples of P-BQ-0 %, P-BQ-25 %, P-BQ-50 %, P-BQ-75 %, and P-BQ-100 %. The shift of the ^{1}H spectrum implies that the BQ molecules form the hydrogen bonding coupling with PANI, thereby inducing a change in the hydrogen peak within the ^{1}H NMR spectrum. This result provides cogent evidence for the formation of hydrogen bonding coupling between BQ and PANI.

To elucidate the formation of hydrogen bonding coupling, a comprehensive analysis was conducted on the physical characteristics of five P-BQ samples, utilizing the PDF, FTIR, and XPS. In the low distance range of PDF results in Fig. 2a (blue part of Fig. S3), the PDF results manifest that the BQ molecule is stretched as it is evinced by the variation of PDF peaks from position ① to position ②. This verifies that the BQ molecule is attracted by PANI via hydrogen bonding coupling. To be more specific, the pristine BQ (P-BQ-0 %) delivers two peaks (Fig. 2a, position ①) with atom distances of 3.58 Å and 3.94 Å (Fig. S4a)

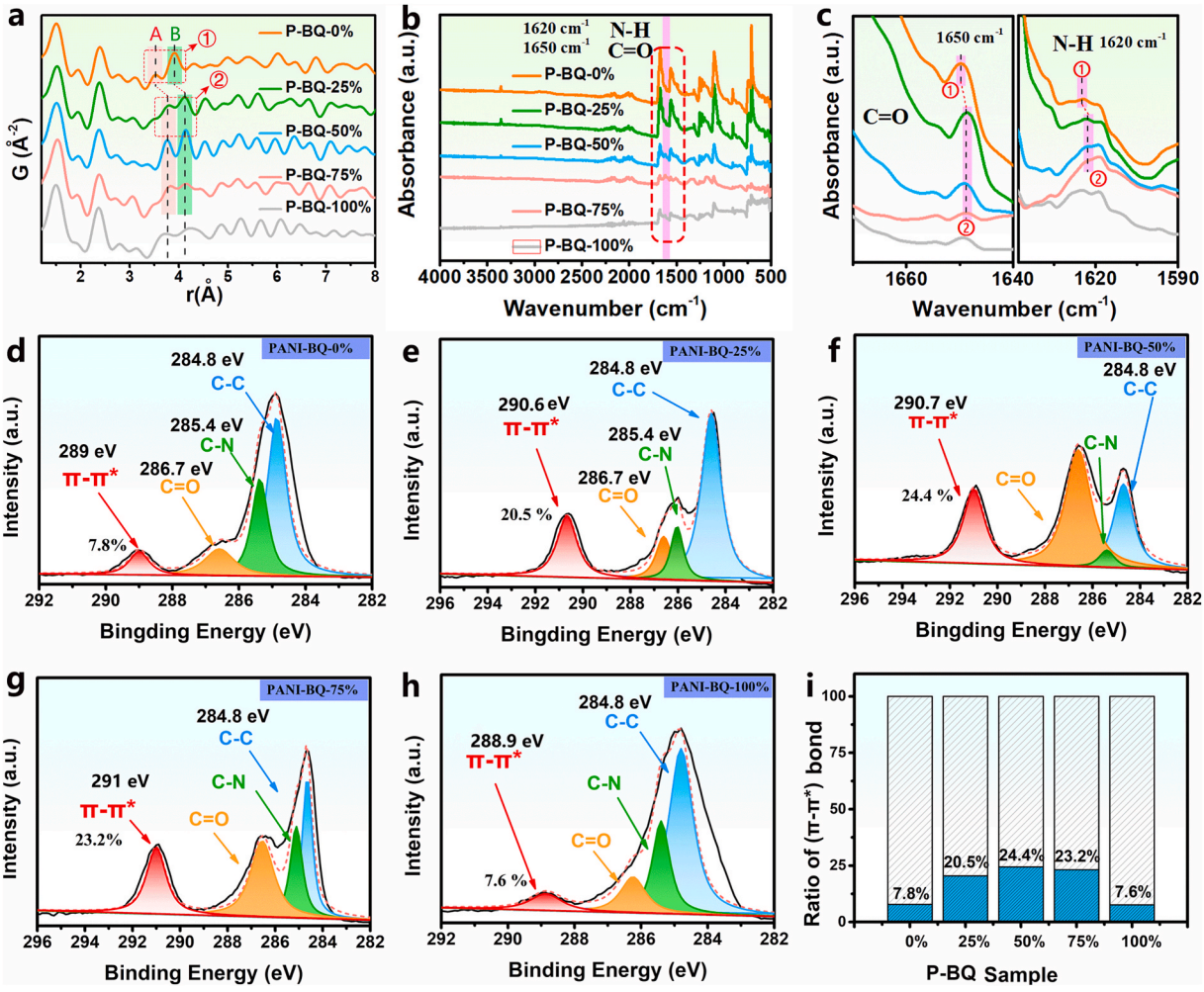

Fig. 2. Revealing hydrogen bonding coupling via physical characteristics of P-BQ. (a) PDF spectra (b, c) FTIR spectra and (d, e, f, g, h) XPS of P-BQ with five samples. (i) Bar chart comparison of the π-π bond with five samples.

belonging to the atom distances between oxygen and two carbon atoms. When different ratios of PANI (25 %, 50 %, 75 %) are added to BQ, the two peaks of these samples move from position ① to position ② as shown in the red box in Fig. 2a, indicating that the distance of two atoms in BQ is stretched to 3.76 Å and 4.16 Å (Fig. S4b). The stretching of two atoms might be attributed to the formation of hydrogen bonding coupling between PANI and BQ. Moreover, it should be emphasized that for the P-BQ-100 %, its two peaks deviate towards both sides rather than being at position ①. Similar results are also observed in infrared spectra results. The N-H bond shows a vibration around 1620 cm^{-1} (Fig. 2b, c) when it moves from position ① to position ② (Fig. 2c), illustrating that the N-H bond is stretched when the hydrogen bonding coupling is formed between BQ and PANI. Meanwhile, the C=O bond (around 1650 cm^{-1}) moves from ① to ② (Fig. 2c), suggesting that the C=O bond stretches when BQ and PANI form hydrogen-bonding coupling. The results of PDF and FTIR unveil that BQ molecules establish a connection with PANI via the hydrogen bonding coupling between C=O and N-H.

To explicate the molecular configuration relationship of BQ and PANI, XPS was utilized to analyze the structure of P-BQ. The full XPS spectra of five samples are shown in Fig. S5. Within the C1s peaks of the XPS spectra (Fig. 2d-h), the proportions of π-π bonds (the π-π bond position is around ~ 290 eV)[44,45] for five samples (P-BQ-0 %, P-BQ-25 %, P-BQ-50 %, P-BQ-75 %, P-BQ-100 %) are 7.8 %, 20.5 %, 24.4 %, 23.2 %, 7.6 %, respectively. Three samples (P-BQ-25 %, P-BQ-50 %, P-BQ-75 %) exhibit a high proportion of the π-π bonds (Fig. 2e, f, g), which evinces the establishment of π-π bonds when BQ is mixed with PANI. On the contrary, for the pure BQ (P-BQ-0 %, Fig. 2d) and pure PANI (P-BQ-100 %, Fig. 2 h) samples, the proportion of the π-π bonds is relatively low, suggesting that pure BQ and PANI samples do not inherently form a significant amount of π-π bonds by themselves. As a result, the formation of π-π bonds provides cogent evidence to attest that P-BQ forms a uniform structure with π-π stacking at the molecular level shown in Fig. S6. The ratio of the π-π stacking illustrates the highest proportion when the addition of PANI is 50 % in Fig. 2i, representing an ideal ratio of PANI addition. In summary, these results disclose that BQ and PANI establish a connected architecture via the electrostatic attraction of the C=O and the N-H at the molecular level, simultaneously, forming a uniform mixed structure via π-π stacking, which is beneficial for the conductivity enhancement of BQ materials.

To investigate the specific function of PANI in conductivity enhancement of BQ, SEM and an optical microscope were applied to analyze the morphological information of P-BQ samples. As shown in Fig. S7a, Fig. S7b, as the addition of PANI ranges from 0 % to 100 % in increments of 25 %, the particle sizes undergo a transformation from large crystallized structures to small non-crystallized particles among the five samples (crystallized particle ~ 200 μm → crystallized particle ~ 50 μm → non crystallized particle ~ 5 μm → non crystallized particle ~ 0.5 μm → non crystallized particle ~ 0.1 μm), signifying that the PANI precludes the BQ from forming the large-size crystallized particles. Similar results are presented in the optical microscope observation. The regularly arranged streak pattern is observed in the P-BQ-0 % sample (Fig. S7c), suggesting that the original BQ represents a crystallized structure (~200 μm). The particle size gradually becomes smaller when the ratio of PANI addition increases (Fig. S7c), which is in accordance with SEM results. In the morphology study of P-BQ, the crystal particle size of P-BQ changes from a relatively large size to a relatively small size, which attests that the crystal structure of BQ molecules (Fig. 3a) is rearranged by the PANI chains via the electrostatic attraction of hydrogen bonding coupling (Fig. 3b). As a result, the morphology study of P-BQ certifies that the addition of PANI is beneficial for diminishing the size of BQ and rearranging BQ molecules to graft onto PANI chains, which is capable of enhancing the conductivity of P-BQ.

To further study the configuration of P-BQ at the molecular level, XRD and Raman were applied to detect the crystal structure information of the aforementioned five P-BQ samples. The XRD peaks of P-BQ in Fig. S8a gradually decline as the addition of PANI increases (0 %, 25 %, 50 %, 75 %, 100 %). This is attributed to the fact that the PANI attenuates the crystal structure of BQ and rearranges the BQ molecules at the molecular level. Simultaneously, the Raman testing results indicate that the intensity of Raman peaks decreases as the additional amount of PANI increases, which further proves the gradual reduction of the material crystallinity (Fig. S8b). These results certify that the BQ molecules are rearranged by the EICR strategy at the molecular level instead of aggregating themselves.

Commonly, the BQ has the crystal structure as shown in Fig. S9 in the a, b, c directions, but the BQ with crystal structure exhibits very low conductivity, due to the fact that there is a poor connection between non-conductive covalent compounds of BQ. This means that only the

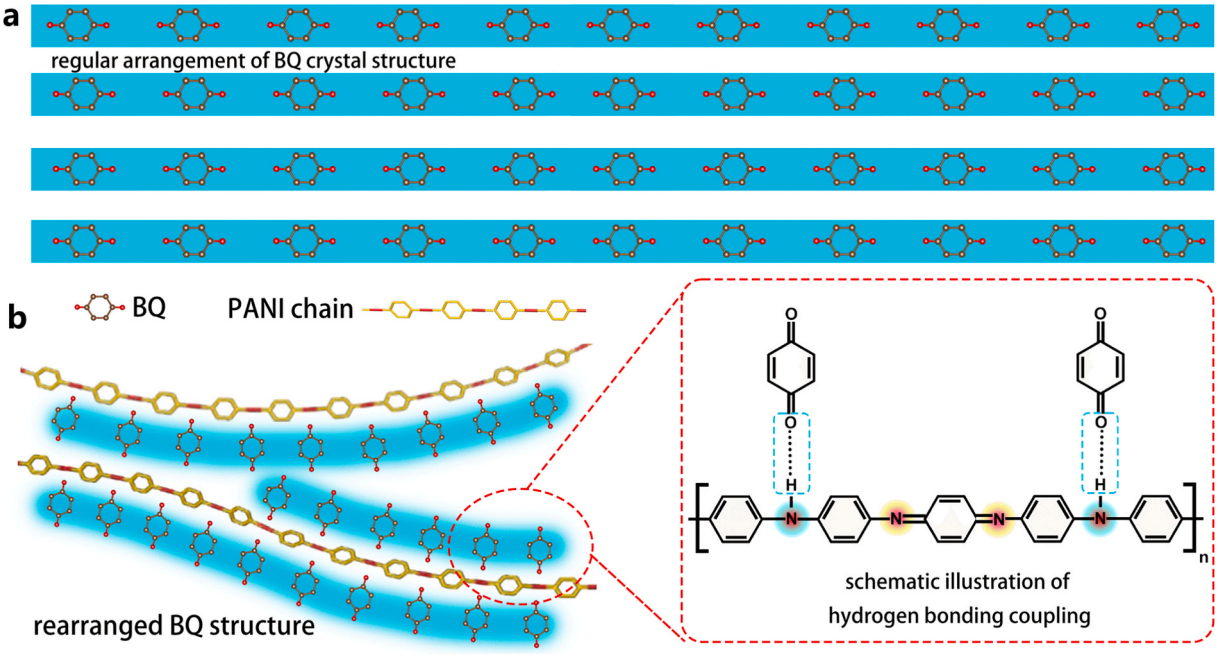

Fig. 3. (a) Crystal structure of BQ particle. (b) Schematic illustration of hydrogen bonding coupling for P-BQ.

minuscule molecules on the surface layer of BQ particles (yellow part in Fig. S10) participate in the electrochemical reaction. The interior molecules (blue part in Fig. S10) of BQ particles are difficult to sufficiently involve in electrochemical reactions. Therefore, the larger the crystal particles of the BQ electrode are, the less sufficiently the electrochemical reaction proceeds. In this work, the crystal structure of BQ is successfully rearranged via the EICR strategy at the molecular level, manifesting enhanced electronic conductivity and ionic conductivity. This characteristic is highly beneficial for the electrochemical reaction of the P-BQ electrode as it enhances charge transfer kinetics and ion diffusion processes. The obtained data clearly show that after the addition of polyaniline, the electronic conductivity of the material increases to 2.23×10^{-4} S cm^{-1} (PANI-BQ), while the conductivity of the material without polyaniline is 1.18×10^{-7} S cm^{-1} (BQ). This significant difference in electronic conductivity values provides strong experimental evidence for the positive impact of polyaniline on improving the conductivity of the material. This particular molecular configuration of P-BQ provides a conductive network for BQ electrodes at the molecular level, which may proffer an effective stratagem for improving the molecular regulation of organic electrodes.

2.2. Elucidating electrochemical performance of P-BQ half-cell

The electrochemical performance was evaluated in a Swagelok cell as a half-cell (Fig. 4a) with 1 M H_2SO_4 electrolyte. The assembling of the Swagelok cell is shown in Fig. S11. The application of the Swagelok cell diminishes the electrochemical polarization, enabling the accurate assessment of the electrochemical performance of electrode materials (Fig. S12). In the electrochemical study of P-BQ, the implementation of PANI leads to a promising improvement in the specific capacity of the BQ electrode material and delivers the highest discharge capacity performance when PANI addition is 50 % (Fig. 4b). The P-BQ-50 % sample showcases a significant reduction in the electrochemical polarization when it is compared with the BQ sample, presenting the polarization from △0.19 V to △0.15 V in cyclic voltammetry (CV) results (Fig. 4c). The P-BQ-50 % exhibits a high discharge capacity of 150.6 mAh g^{-1} at the current density of 500 mA g^{-1} (Fig. 4d), whereas P-BQ-0 % only presents a discharge capacity of 7.4 mAh g^{-1} under the same testing condition (Fig. 4 g). In Fig. 4e, the combination of P-BQ and PANI gives rise to a conductive network structure. This network, on one hand, augments the conductivity and, on the other hand, facilitates sufficient electrochemical reaction. The synergy of these two aspects leads to the manifestation of superior capacity in P-BQ.

The subpar electrochemical performance of BQ is ascribed to the fact that BQ possesses intrinsically poor electronic conductivity and only a thin layer of BQ particles participates in the electrochemical process (Fig. S10), resulting in an insufficient electrochemical reaction of the electrode (Fig. 4 h). Consequently, BQ exhibits poor electrochemical performance. The poor conductivity of BQ is also reflected in EIS results (Fig. 4f). The interface resistance of charge transfer (Rct)[46] of P-BQ-50 % is 3.2 Ω but the Rct of P-BQ-0 % is 28 Ω, which suggests that P-BQ-0 % displays high interfacial resistance during electrochemical reaction. As a result, the conductivity of BQ is successfully advanced via PANI. This EICR strategy serves as an efficacious approach for the conductivity

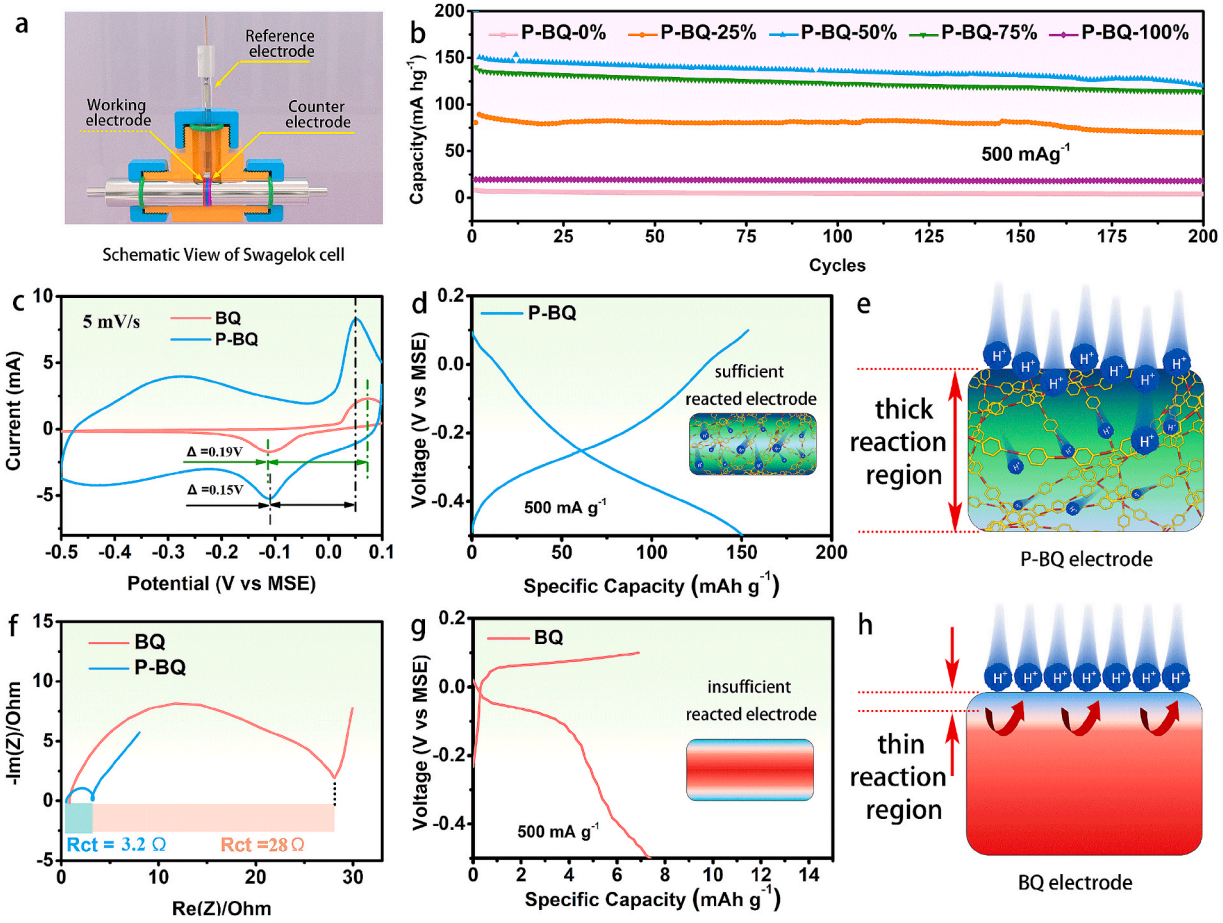

Fig. 4. Disclosing electrochemical performance for P-BQ half-cell. (a) Schematic illustration of electrode position in Swagelok cell. (b) Comparison of the specific discharge capacity of the P-BQ with five samples. (c) CV curves of the P-BQ-0% and P-BQ-50%. (d) GCD (galvanostatic charge/discharge) curves of the P-BQ-50% and (e) its schematic illustration of reaction region during electrochemical reaction. (f) EIS plot of the P-BQ-0% and P-BQ-50%. (g) GCD curves of the P-BQ-0% and (h) schematic illustration of the reaction region thereof.

modification of organic electrodes, thereby facilitating the large-scale application of organic electrodes within PBs.

2.3. Unveiling the proton storage in P-BQ

To unveil the mechanism of proton storage in P-BQ, the in-situ approach was applied to reveal detailed information during the charge and discharge process. The in-situ cell (Fig. 5a) is assembled with P-BQ-50 % as a cathode and P-2ClAQ (PANI-2-Chloroanthraquinone) as an anode, and the digital photo of the testing device is shown in Fig. 5b. P-2ClAQ proves beneficial as it, when combined with polyaniline, can effectively enhance the electrode's conductivity and stability during in-situ tests. In the 3D plot of the in-situ FTIR investigation (Fig. 5c), two peaks around 3600 cm^{-1} (O-H) and 1880 cm^{-1} (C=O) appear, manifesting that the mechanism of proton storage for P-BQ involves functional group variation between C=O and C-OH corresponding with BQ and BQH (hydrogenated benzoquinone). These two peaks continuously appear five times in Fig. 5c, indicating that the in-situ results are replicable. The 2D plots of the in-situ FTIR investigation show similar results. During the charge and discharge process (Fig. 5d), three peaks around 3600 cm^{-1}, 1880 cm^{-1}, and 1270 cm^{-1} were observed in 2D plots (Fig. 5e, 5f). These peaks are attributed to the vibrations of O-H, C=O, and C-O function groups, respectively, indicating that the mechanism of proton storage in BQ undergoes a shift between BQ and BQH during the electrochemical process. It is noteworthy that the peak around 1620 cm^{-1} (N-H) remains unchanged (Fig. 5f) during the electrochemical reaction, denoting that PANI is not engaged in the electrochemical reaction within the P-BQ system.

From the in-situ Raman results (Fig. 5 g, Fig. 5 h), similar mechanisms are observed, with a peak around 3000 cm^{-1} (Fig. 5 h) appearing during the charge/discharge process (Fig. 5 g). This peak is attributed to the vibration of OH. The study on the electrochemical reaction mechanism of P-BQ reveals that BQ shifts to BQH during the discharging process and changes back to BQ during the charging process (Fig. S13). In this section, the electrochemical reaction of BQ is manifested as a functional group transition from C=O to C-OH during the charge/discharge process. The N-H peak[47] demonstrates no change around 1620 cm^{-1}, which indicates that PANI does not influence the electrochemical reaction of BQ. XRD patterns (Fig. S14) clearly show that the crystal structure remains highly consistent before and after cycling, indicating no phase transformation during the process.

2.4. Enunciating practical application of P-BQ full-cell

It is imperative to investigate the full-cell performance of PBs because the half-cell is excessively costly and highly complex for the practical application of PBs. The half-cell necessitates a reference electrode or hydrogen as an anode for operation. The reference electrode requires stringent working conditions and a complex cell enclosure, which is not feasible in practical applications[48,49]. In the case where hydrogen is employed as the anode, hydrogen anode will occupy a substantial volume and pose a high risk, which is contrary to the safety requirements of PBs[50–55]. If the two-electrode full-cell is available, the structure of PBs will be simplistic with high economic viability, and the volume of PBs will be small while possessing high energy density. Currently, the majority of reports related to proton batteries just stay at the stage of examining the three-electrode facet. Consequently, we propound that it is imperative to investigate the full-cell performance within the realm of PBs research. Moreover, if the pouch cell performance is examined for further exploration, it holds substantial significance for the practical application of PBs.

In the full-cell study, the coin cell (Fig. 6a) was constituted of P-BQ//H_2SO_4//P-2ClAQ as depicted in Fig. 6b, presenting a structure of simplicity and providing a referential model for the energy storage in PBs. The titanium material can stably operate within a much broader range of −1.2 V to above 4 V. For the identification of 2ClAQ, the anode material characteristics are provided in Fig. S 15–17. The 2ClAQ is selected as the anode for its low discharge potential (−0.6 V) in Fig. S18 In P-BQ//H_2SO_4//P-2ClAQ full-cell, the CV curves (Fig. 6c) show almost no change for 10 cycles, indicating that the electrode is quite stable. Since polyaniline (PANI) itself has supercapacitor properties, after the BQ material is combined with PANI, the composite material can provide

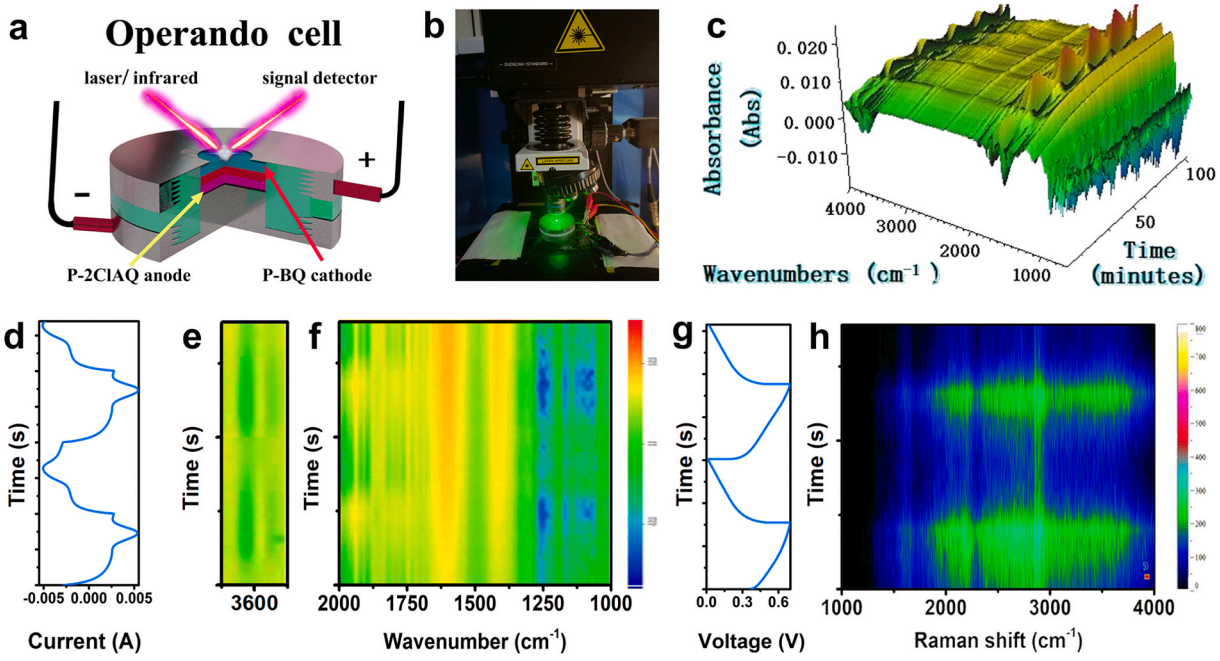

Fig. 5. Explicating proton-storage mechanism of P-BQ by in-situ characterization of Raman and FTIR. (a) Schematic illustration of in-situ FTIR and in-situ Raman investigation in the in-situ cell. (b) Digital photo of in-situ Raman device. (c) 3D plot of in-situ FTIR spectra for P-BQ-50%. (d) Current and time curves of P-BQ-50% in cyclic voltammetry (CV) relating to (e, f) 2D plot of in-situ FTIR spectra. (g) Voltage and time curves of P-BQ-50% corresponding to (h) in-situ Raman testing results.

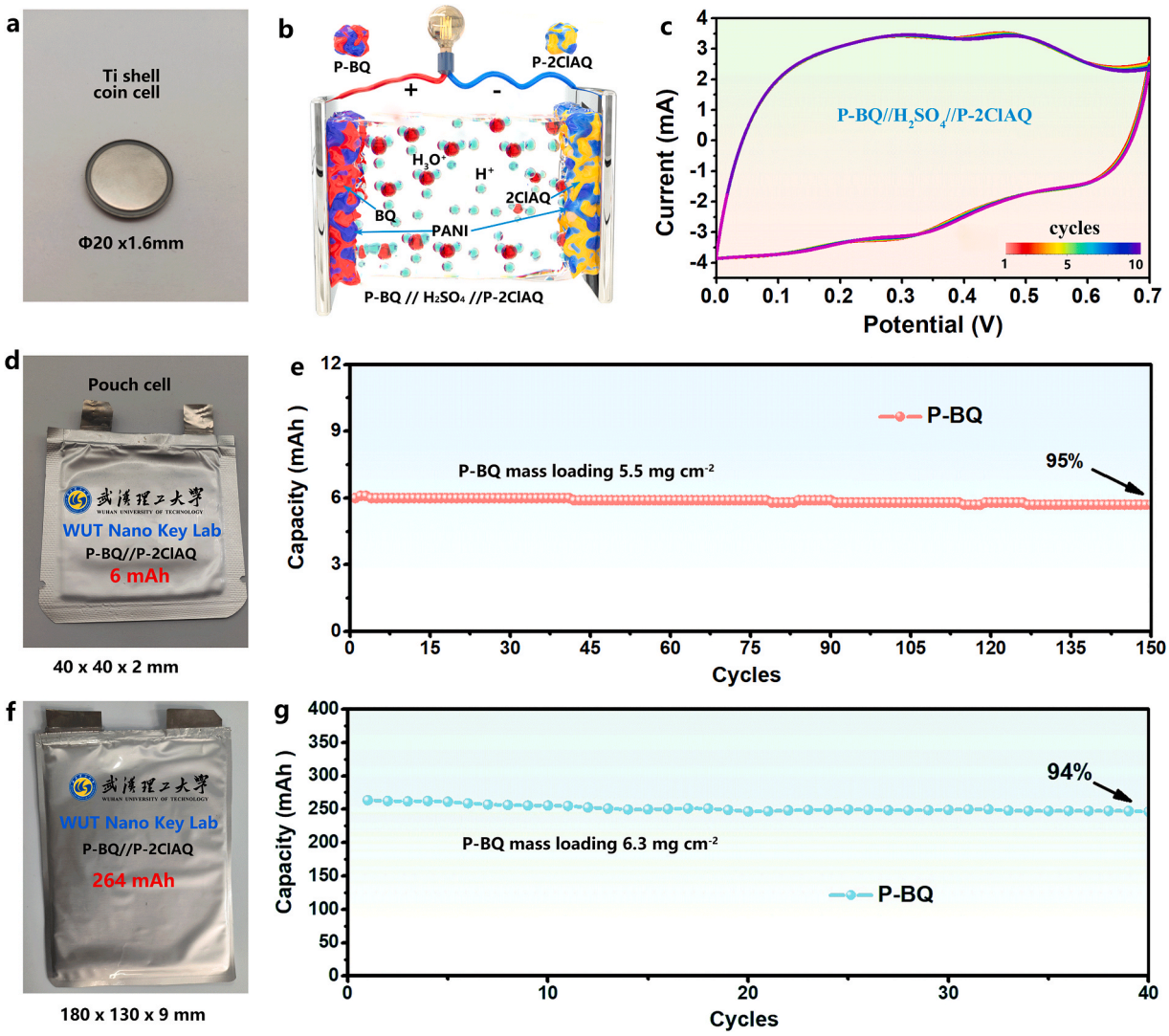

Fig. 6. Expounding electrochemical performance of P-BQ full-cell. (a) Digital photo of Ti coin cell. (b) Schematic illustration of P-BQ full-cell (P-BQ//H_2SO_4//P-2ClAQ). (c) CV curves of P-BQ at 10 mV s^{-1}. (d) Digital photo and (e) cycling performance of small-size pouch cell. (f) Digital photo and (g) cycling performance of large-size pouch cell.

both electrochemical capacity and supercapacitor capacity. In the CV plot in Fig. 6c, the presence of a rectangular region suggests that the proton battery full cell, after the addition of polyaniline, maybe a hybrid energy storage device incorporating both capacitive and battery-like characteristics.

To further evaluate the practicability of the P-BQ electrode, the pouch cells were assembled as P-BQ//H_2SO_4//P-2ClAQ in Fig. 6d, 6f. Both pouch cells were assembled with the Ti current collector and the electrolyte was 1 M H_2SO_4. A single-layer pouch cell with a size of 40 mm × 40 mm × 2 mm and a large-size winding-formed pouch cell with a size of 180 mm × 130 mm × 9 mm were both successfully assembled and tested. The voltage window for full-cell was tested at 0 ~ 0.7 V, and the current density was 100 mA g^{-1}. For the single-layer pouch cell, its maximum capacity is 6 mAh (Fig. 6e), and the capacity retention is 95 % (5.7 mAh) in comparison with the maximum value (6 mAh) for 150 cycles. Notably, for the first time, the large-size proton pouch cell (Fig. 6f) is achieved with a maximum capacity of 264 mAh in PBs and delivers capacity retention of 94 % for 40 cycles (Fig. 6 g). The large-size pouch cell (P-BQ//H_2SO_4//P-2ClAQ) showcases the highest capacity among current reports (Fig. S19). Up to now, high-capacity pouch cells in PBs have been rarely explored (Table S1), so the success of high-capacity pouch cells represents the practical potential of P-BQ electrodes and provides a referable model in the practical application of PBs.

3. Conclusion

In conclusion, this work has developed a facile EICR strategy for enhancing the conductivity of organic electrodes in aqueous proton batteries. The EICR strategy, mediated by hydrogen bonding coupling between C=O in BQ and N-H bonds in PANI, has been thoroughly verified by multiple techniques including DFT, NMR, PDF, and FTIR. This molecular-level manipulation successfully rearranges the original poor conductive crystal structure of the electrode to a well-conductive one, resulting in a significant reduction in electrochemical polarization (from △0.19 V to △0.15 V) and charge-transfer interfacial resistance (from 28 Ω to 3.2 Ω). It has been demonstrated that the addition of PANI effectively prevents BQ from forming large-sized crystallized particles and promotes the rearrangement of BQ molecules, thus enhancing the conductivity of the P-BQ. For the first time, a high capacity (264 mAh) pouch cell is achieved, which unfolds promising potentiality for the practical application of PBs. This research not only presents a practical strategy for augmenting the conductivity of organic electrodes but also uncovers the underlying scientific mechanism of the

EICR strategy, thereby providing a theoretical foundation for molecular regulation and a practicable example for the large-scale application in PBs.

CRediT authorship contribution statement

Jianyong Zhang: Writing – review & editing, Writing – original draft, Validation, Methodology, Investigation, Conceptualization. **Jingyuan Yu:** Formal analysis, Data curation. **Wenwei Zhang:** Data curation, Conceptualization. **Ahmed Eissa Abdelmaoula:** Writing – review & editing, Writing – original draft, Funding acquisition. **Chunhua Han:** Writing – review & editing, Writing – original draft, Methodology. **Zhenzhen Dou:** Investigation, Methodology. **Feng Liang:** Writing – review & editing, Writing – original draft, Methodology, Funding acquisition. **Lin Xu:** Writing – review & editing, Writing – original draft, Funding acquisition.

Declaration of competing interest

The authors declare that they have no known competing financial interests or personal relationships that could have appeared to influence the work reported in this paper.

Acknowledgments

This work was supported by the National Natural Science Foundation of China, China (52272234, 52172233); the National Key Research and Development Program of China, China (2020YFA0715000); the International Science and Technology Cooperation Program of Hubei Province, China and Egypt (2024EHA039); the Independent Innovation Project of Hubei Longzhong Laboratory, China (2022ZZ-20).

Appendix A. Supplementary data

Supplementary data to this article can be found online at https://doi.org/10.1016/j.cej.2025.161930.

Data availability

Data will be made available on request.

References

[1] X. Wang, C. Bommier, Z. Jian, Z. Li, R.S. Chandrabose, I.A. Rodriguez-Perez, P. A. Greaney, X. Ji, Hydronium-ion batteries with perylenetetracarboxylic dianhydride crystals as an electrode, Angew. Chem. Int. Ed. 56 (11) (2017) 2909, https://doi.org/10.1002/anie.201700148.
[2] Y. Shi, Y. Chen, L. Shi, K. Wang, B. Wang, L. Li, Y. Ma, Y. Li, Z. Sun, W. Ali, S. Ding, An overview and future perspectives of rechargeable zinc batteries, Small 16 (23) (2020) e2000730, https://doi.org/10.1002/smll.202000730.
[3] A. Nimkar, M.S. Chae, S. Wee, G. Bergman, B. Gavriel, M. Turgeman, F. Malchik, M.D. Levi, D. Sharon, M.R. Lukatskaya, N. Shpigel, D. Mandler, What about manganese? Toward rocking chair aqueous Mn-ion batteries, ACS Energy Lett. 7 (12) (2022) 4161, https://doi.org/10.1021/acsenergylett.2c02242.
[4] Y.K. Xu, X.Y. Wu, X.L. Ji, The renaissance of proton batteries, Small Struct. 2 (5) (2021) 2000113, doi: ARTN 200011310.1002/sstr.202000113.
[5] J.-L. Yang, J.-M. Cao, X.-X. Zhao, K.-Y. Zhang, S.-H. Zheng, Z.-Y. Gu, X.-L. Wu, Advanced aqueous proton batteries: working mechanism, key materials, challenges and prospects, EnergyChem 4 (6) (2022) 100092, https://doi.org/10.1016/j.enchem.2022.100092.
[6] M.M. Shi, P. Das, Z.S. Wu, T.G. Liu, X.Y. Zhang, Aqueous organic batteries using the proton as a charge carrier, Adv. Mater. 35 (42) (2023) 2302199, https://doi.org/10.1002/adma.202302199.
[7] T. Xu, D. Wang, Z. Li, Z. Chen, J. Zhang, T. Hu, X. Zhang, L. Shen, Electrochemical proton storage: from fundamental understanding to materials to devices, Nano-Micro Lette 14 (1) (2022) 126, https://doi.org/10.1007/s40820-022-00864-y.
[8] H.C. Guo, C. Zhao, An emerging chemistry revives proton batteries, Small Methods 8 (6) (2024) 2300699, https://doi.org/10.1002/smtd.202300699.
[9] J. Li, H.H. Yan, C.W. Xu, Y.W. Liu, X.K. Zhang, M.T. Xia, L.Y. Zhang, J. Shu, Insights into host materials for aqueous proton batteries: structure, mechanism and prospect, Nano Energy 89 (2021) 106400, https://doi.org/10.1016/j.nanoen.2021.106400.
[10] L. Zhou, L. Liu, Z. Hao, Z. Yan, X.-F. Yu, P.K. Chu, K. Zhang, J. Chen, Opportunities and challenges for aqueous metal-proton batteries, Matter 4 (4) (2021) 1252, https://doi.org/10.1016/j.matt.2021.01.022.
[11] C. Huang, W. Zhang, W. Zheng, Proton batteries shape the next energy storage, Energy Storage Mater. 61 (2023) 102913, https://doi.org/10.1016/j.ensm.2023.102913.
[12] Z. Su, H. Guo, C. Zhao, Rational design of electrode–electrolyte interphase and electrolytes for rechargeable proton batteries, Nano-Micro Letters 15 (1) (2023) 1596, https://doi.org/10.1007/s40820-023-01071-z.
[13] R. Emanuelsson, M. Sterby, M. Stromme, M. Sjodin, An all-organic proton battery, J. Am. Chem. Soc. 139 (13) (2017) 4828, https://doi.org/10.1021/jacs.7b00159.
[14] Y. Xu, Y. Zheng, C. Wang, Q. Chen, An all-organic aqueous battery powered by adsorbed quinone, ACS Appl. Mater. Interfaces 11 (26) (2019) 23222, https://doi.org/10.1021/acsami.9b05159.
[15] T. Sun, H. Du, S. Zheng, J. Shi, X. Yuan, L. Li, Z. Tao, Bipolar organic polymer for high performance symmetric aqueous proton battery, Small Methods 5 (8) (2021) e2100367, https://doi.org/10.1002/smtd.202100367.
[16] J.Z. Yu, J. Li, Z.Y. Leong, D.S. Li, J. Lu, Q. Wang, H.Y. Yang, A crystalline dihydroxyanthraquinone anodic material for proton batteries, Mater. Today Energy 22 (2021) 100872, https://doi.org/10.1016/j.mtener.2021.100872.
[17] T. Tomai, S. Mitani, D. Komatsu, Y. Kawaguchi, I. Honma, Metal-free aqueous redox capacitor via proton rocking-chair system in an organic-based couple, Sci. Rep. 4 (2014) 3591, https://doi.org/10.1038/srep03591.
[18] K. Nueangnoraj, T. Tomai, H. Nishihara, T. Kyotania, I. Honmaa, An organic proton battery employing two redox-active quinones trapped within the nanochannels of zeolite-templated carbon, Carbon 107 (2016) 831, https://doi.org/10.1016/j.carbon.2016.06.096.
[19] S. Suematsu, K. Naoi, Quinone-introduced oligomeric supramolecule for supercapacitor, J. Power Sources 97 (2001) 816, https://doi.org/10.1016/S0378-7753(01)00735-2.
[20] F. Yue, Z. Tie, S. Deng, S. Wang, M. Yang, Z. Niu, An ultralow temperature aqueous battery with proton chemistry, Angew. Chem. Int. Ed. 60 (25) (2021) 13882, https://doi.org/10.1002/anie.202103722.
[21] Y. Liang, Y. Jing, S. Gheytani, K.Y. Lee, P. Liu, A. Facchetti, Y. Yao, Universal quinone electrodes for long cycle life aqueous rechargeable batteries, Nat. Mater. 16 (8) (2017) 841, https://doi.org/10.1038/nmat4919.
[22] C. Strietzel, M. Sterby, H. Huang, M. Stromme, R. Emanuelsson, M. Sjodin, An aqueous conducting redox-polymer-based proton battery that can withstand rapid constant-voltage charging and sub-zero temperatures, Angew. Chem. Int. Ed. 59 (24) (2020) 9631, https://doi.org/10.1002/anie.202001191.
[23] M. Zhu, L. Zhao, Q. Ran, Y. Zhang, R. Peng, G. Lu, X. Jia, D. Chao, C. Wang, Bioinspired catechol-grafting PEDOT cathode for an all-polymer aqueous proton battery with high voltage and outstanding rate capacity, Adv. Sci. 9 (4) (2022) e2103896, https://doi.org/10.1002/advs.202103896.
[24] X. Wang, J. Zhou, W. Tang, Poly(dithieno[3,2-b:2',3'-d]pyrrole) twisting redox pendants enabling high current durability in all-organic proton battery, Energy Storage Mater. 36 (2021) 109, https://doi.org/10.1016/j.ensm.2020.12.016.
[25] A.M. Navarro-Suárez, J. Carretero-González, T. Rojo, M. Armand, Poly(quinone-amine)/nanocarbon composite electrodes with enhanced proton storage capacity, J. Mater. Chem. A 5 (44) (2017) 23292, https://doi.org/10.1039/c7ta08489g.
[26] H. Wang, R. Emanuelsson, C. Karlsson, P. Jannasch, M. Stromme, M. Sjodin, Rocking-chair proton batteries with conducting redox polymer active materials and protic ionic liquid electrolytes, ACS Appl. Mater. Interfaces 13 (16) (2021) 19099, https://doi.org/10.1021/acsami.1c01353.
[27] T. Sun, H. Du, S. Zheng, J. Shi, Z. Tao, High power and energy density aqueous proton battery operated at −90 °C, Adv. Funct. Mater. 31 (16) (2021) 2010127, https://doi.org/10.1002/adfm.202010127.
[28] Z.W. Guo, J.H. Huang, X.L. Dong, Y.Y. Xia, L. Yan, Z. Wang, Y.G. Wang, An organic/inorganic electrode-based hydronium-ion battery, Nat. Commun. 11 (1) (2020) 959, doi: ARTN 95910.1038/s41467-020-14748-5.
[29] Z. Tie, L. Liu, S. Deng, D. Zhao, Z. Niu, Proton insertion chemistry of a zinc-organic battery, Angew. Chem. Int. Ed. 59 (12) (2020) 4920, https://doi.org/10.1002/anie.201916529.
[30] J. Qiao, M. Qin, Y.M. Shen, J. Cao, Z. Chen, J. Xu, A rechargeable aqueous proton battery based on a dipyridophenazine anode and an indium hexacyanoferrate cathode, Chem. Commun. 57 (35) (2021) 4307, https://doi.org/10.1039/d1cc01486b.
[31] H. Fan, K. Liu, X. Zhang, Y. Di, P. Liu, J. Li, B. Hu, H. Li, M. Ravivarma, J. Song, Spatial structure regulation towards armor-clad five-membered pyrroline nitroxides catholyte for long-life aqueous organic redox flow batteries, eScience 1 (2023) 100202, https://doi.org/10.1016/j.esci.2023.100202.
[32] T. Sun, Q. Nian, H. Du, S. Zheng, D. Han, Z. Tao, Aqueous proton battery stably operates in mild electrolyte and low-temperature conditions, J. Mater. Chem. A 10 (33) (2022) 17288, https://doi.org/10.1039/d2ta04272j.
[33] Z. Song, H. Zhou, Towards sustainable and versatile energy storage devices: an overview of organic electrode materials, Energy Environ. Sci. 6 (8) (2013) 2280, https://doi.org/10.1039/c3ee40709h.
[34] S. Chen, C. Yu, C. Wei, Z. Jiang, Z. Zhang, L. Peng, S. Cheng, J. Xie, Unraveling electrochemical stability and reversible redox of y-doped Li_2ZrCl_6 solid electrolytes, Energy Mater. Adv. 4 (2023), https://doi.org/10.34133/energymatadv.0019.
[35] P.-Z. Ge, X.-G. Tang, Q.-X. Liu, Y.-P. Jiang, X.-B. Guo, Superior energy and power density realized in $Pb(Hf_{1-x}Ti_x)O_3$ system at low electric field, Energy Mater. Adv. 4 (2023), https://doi.org/10.34133/energymatadv.0025.

[36] H. Jing, H. Xing, B. Li, Y. Han, Spherical particles growth with dynamic oscillation during lithium electrodeposition, Energy Mater. Adv. 4 (2023), https://doi.org/10.34133/energymatadv.0018.
[37] N.C. Dargily, R. Thimmappa, M.C. Devendrachari, M.O. Thotiyl, An air chargeable hydrogen battery by reversible electrochemical trapping of the protons, Green Chem. 24 (22) (2022) 8820, https://doi.org/10.1039/d2gc02927h.
[38] S. Liu, S. Jin, T.L. Jiang, M. Sajid, J.W. Xu, K. Zhang, Y.P. Fan, Q. Peng, X.H. Zheng, Z.H. Xie, Z.C. Liu, Z.X. Zhu, X.Y. Wang, Q.S. Nian, J.H. Chen, K. Li, C.Y. Shen, W. Chen, Aqueous organic hydrogen gas proton batteries with ultrahigh-rate and ultralow-temperature performance, Nano Lett. 23 (20) (2023) 9664, https://doi.org/10.1021/acs.nanolett.3c01304.
[39] X. Yang, Y. Ni, Y. Lu, Q. Zhang, J. Hou, G. Yang, X. Liu, W. Xie, Z. Yan, Q. Zhao, J. Chen, Designing quinone-based anodes with rapid kinetics for rechargeable proton batteries, Angew. Chem. Int. Ed. 61 (39) (2022) e202209642, https://doi.org/10.1002/anie.202209642.
[40] L. Li, X. Zhang, Y. Lu, X. Chen, H. Cheng, Y. Lu, Recent advances and future perspectives of membranes in iron-based aqueous redox flow batteries, Energy Mater. Adv. 5 (2024), https://doi.org/10.34133/energymatadv.0118.
[41] J. Liang, X. Li, C. Wang, J.T. Kim, R. Yang, J. Wang, X. Sun, Current status and future directions in environmental stability of sulfide solid-state electrolytes for all-solid-state batteries, Energy Mater. Adv. 4 (2023), https://doi.org/10.34133/energymatadv.0021.
[42] Z. Pan, K. Li, L. Sun, Y. Li, Z. Zhang, Y. Qian, W. Chen, A high-concentration edge-nitrogen-doped porous carbon anode via template free strategy for high-performance potassium-ion hybrid capacitors, Energy Mater. Adv. 5 (2024), https://doi.org/10.34133/energymatadv.0080.
[43] S. Isikli, M. Lecea, M. Ribagorda, M.C. Carreño, R. Díaz, Influence of quinone grafting via Friedel–crafts reaction on carbon porous structure and supercapacitor performance, Carbon 66 (2014) 654, https://doi.org/10.1016/j.carbon.2013.09.062.
[44] P. Huang, T. Xiong, S. Zhou, H. Yang, Y. Huang, M.S.J.T. Balogun, Y. Ding, Advanced tri-layer carbon matrices with π–π stacking interaction for binder-free lithium-ion storage, ACS Appl. Mater. Interfaces 13 (14) (2021) 16516, https://doi.org/10.1021/acsami.1c02645.
[45] G. Aimaiti, Y. Zou, Y. Ma, Y. Shi, K. Qi, W. Zhan, Z. Qian, Z. Liu, Y. Dong, "Frozen" π-π stacking on perylene diimide molecules induces oxygen vacancies synergistic activation of persulfate towards degradation of tetracycline, Chem. Eng. J. 496 (2024) 153852, https://doi.org/10.1016/j.cej.2024.153852.
[46] L. Zhang, K. Zhao, Y. Luo, Y. Dong, W. Xu, M. Yan, W. Ren, L. Zhou, L. Qu, L. Mai, Acetylene black induced heterogeneous growth of macroporous Co_3O_4 nanosheets for high-rate pseudocapacitive lithium-ion battery anodes, ACS Appl. Mater. Interfaces 8 (11) (2016) 7139, https://doi.org/10.1021/acsami.6b00596.
[47] M.K. Tufail, P. Zhai, M. Jia, N. Zhao, X. Guo, Design of solid electrolytes with fast ion transport: Computation-driven and practical approaches, Energy Mater. Adv. 4 (2023), https://doi.org/10.34133/energymatadv.0015.
[48] J. Zhang, J. Zhang, X. Ou, C. Wang, C. Peng, B. Zhang, Enhancing high-voltage performance of Ni-rich cathode by surface modification of self-assembled NASICON fast ionic conductor $LiZr_2(PO_4)_3$, ACS Appl. Mater. Interfaces 11 (17) (2019) 15507, https://doi.org/10.1021/acsami.9b00389.
[49] J. Zhang, J. Zhang, J. Liu, Y. Cao, C. Huang, G. Ji, Z. Zhao, X. Ou, B. Zhang, Environmentally phase-controlled stratagem for open framework pyrophosphate anode materials in battery energy storage, J. Mater. Chem. C 9 (29) (2021) 9147, https://doi.org/10.1039/d1tc02106k.
[50] R. Xie, D. Yue, Z. Peng, X. Wei, Achieving energy-saving, continuous redox flow desalination with iron chelate redoxmers, Energy Mater. Adv. 4 (2023), https://doi.org/10.34133/energymatadv.0009.
[51] X. Xu, Y. Wang, C. Wang, B. Cui, C. Wang, Multifunctional C/TiO_2 from MXene/polyaniline for electromagnetic protection and supercapacitor, Energy Mater. Adv. 5 (2024), https://doi.org/10.34133/energymatadv.0070.
[52] J. Zhang, K. Fu, K. Du, C. Wen, J. Yu, C. Han, Y. Hu, L. Xu, Realizing a mildly acidic proton battery via surface functionalization, ACS Energy Lett. 9 (4) (2024) 1853, https://doi.org/10.1021/acsenergylett.3c02571.
[53] J. Zhang, J. Yu, Q. Liu, C. Han, A.E. Abdelmaoula, L. Xu, Inhibition of quinone dissolution via symmetrically polarized effect for ultra-stable proton batteries, Energy Storage Mater 75 (2025) 104055, https://doi.org/10.1016/j.ensm.2025.104055.
[54] C. Wen, J. Zhang, W. Song, F. Shah, H. Zhang, Z. Yang, A.E. Abdelmaoula, L. Xu, High-capacity bismuth phosphate anode with reversible conversion reaction for acid batteries, J. Alloys Compd. 999 (2024) 175033, https://doi.org/10.1016/j.jallcom.2024.175033.
[55] W. Song, J. Zhang, C. Wen, H. Lu, C. Han, L. Xu, L. Mai, Synchronous redox reactions in copper oxalate enable high-capacity anode for proton battery, J. Am. Chem. Soc. 146 (7) (2024) 4762, https://doi.org/10.1021/jacs.3c12710.